Structural Engineering and Mechanics, *Vol. 72, No. 2 (2019) 257-273*
DOI: https://doi.org/10.12989/sem.2019.72.2.257

Three-dimensional modelling of functionally graded beams using Saint-Venant's beam theory

Mourad Khebizi*[1], Hamza Guenfoud[2], Mohamed Guenfoud[2] and Rached El Fatmi[3]

[1]*Department of Civil Engineering, Mentouri University of Constantine, Algeria*
[2]*Civil Engineering and Hydraulic Laboratory, University of Guelma, Algeria*
[3]*University of Tunis El Manar, National Engineering School of Tunis, Tunisia*

(Received December 6, 2018, Revised May 14, 2019, Accepted June 2, 2019)

Abstract. In this paper, the mechanical behaviour of functionally graded material beams is studied using the 3D Saint-Venant's theory, in which the section is free to warp in and out of its plane (Poisson's effects and out-of-plane warpings). The material properties of the FGM beam are distributed continuously through the thickness by several distributions, such as power-law distribution, exponential distribution, Mori-Tanaka schema and sigmoid distribution. The proposed method has been applied to study a simply supported FGM beam. The numerical results obtained are compared to other models in the literature, which show a high performance of the 3D exact theory used to describe the stress and strain fields in FGM beams.

Keywords: functionally graded material; ceramic; metal; modelling; beam; Saint-Venant theory; mechanical behaviour

1. Introduction

Functionally graded materials (FGM) have been widely used in various industries and engineering sectors such as aerospace, aircraft, automobile, defense industries, and biomedical sectors. They are special composites whose composition varies continuously along the thickness of a structure to achieve a required function. Typically, these materials consist of a mixture of ceramic and metal (see Fig. 1), or a combination of different materials. The ceramic constituent provides high-temperature resistance due to its low thermal conductivity. The ductile metal constituent, on the other hand, prevents fracture caused by stresses due to a high temperature gradient in a very short span of time (Pradhan *et al*. 2013). To date, four types of material variations have been proposed such as power-law (P-FGM), sigmoid (S-FGM), Mori-Tanaka (M-FGM), and exponential (E-FGM) models (see Section 2).

The advantages of the functionally graded materials are essentially due to the smooth variations of their mechanical properties along preferential directions, which allow one to preserve high specific stiffness while avoiding the main drawbacks of classical composites (laminated composites) such as the stress discontinuities at the layer-interfaces and the low resistance to thermal shocks (Filippi *et al*. 2015).

The increase in functionally graded materials (FGM) applications requires accurate mathematical models to predict their responses. Recently, several researchers have developed analytical and numerical models in order to study the thermal and mechanical behaviour of FGM structures (micro-beams, beams, plates, etc.). Ziou *et al*. (2016) have studied the static behaviour of functionally graded material beams by a finite element based on the theory of first order shear deformation, in which the Timoshenko kinematics assumption is used. Şimşek (2009) also studied the static behaviour of FGM simply-supported beam by using the Ritz method within the framework of Timoshenko and the higher order shear deformation beam theories.

Belabed *et al*. (2014) presented a higher order shear and normal deformation theory to analyze analytically the free vibration response of functionally graded material (FGM) plates. Pradhan et al. (2013) studied the free vibration of functionally graded beams by Rayleigh-Ritz method; they based in this analysis on the classical and first order shear deformation beam theories.

Sankar (2001) has developed an elasticity solution for a functionally graded beam subjected to sinusoidal transverse loading, he also proposed a simple Euler-Bernoulli type beam theory based on the assumption that the section remains plane and normal to the beam axis.

Recently Filippi *et al*. (2015) have presented a comparison between various analytical models used to perform static analyses of FGM beams.

In recent years, several studies have been conducted on functionally graded nanobeams and nanoplates (Karami *et al*. 2017, Karami *et al*. 2018 a, b, c, Nejad *et al*. 2018, Ebrahimi and Barati 2017, Bağdatli 2015, Kolahchi *et al*. 2015). Kolahchi et al. (2016), Kolahchi et al. (2017 a, b), Hajmohammad et al. (2017), Madani et al. (2016), Hosseini and Kolahci (2018) investigated the analysis of FG carbon nanotubes.

Most of these models are based on simplifying assumptions, such as those related to the kinematics of the beams. For example Euler-Bernoulli and Timoshenko theories in which assume that the section is undeformable

*Corresponding author, Professor
E-mail: Mourad_gc@yahoo.fr

Copyright © 2019 Techno-Press, Ltd.
http://www.techno-press.com/journals/sem&subpage=7 ISSN: 1225-4568 (Print), 1598-6217 (Online)

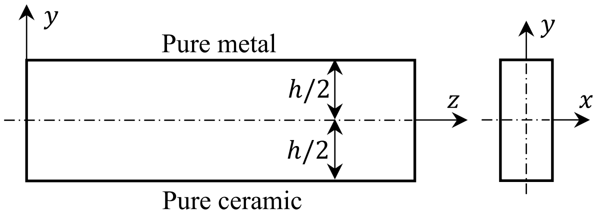

Fig. 1 FGM beam

(for Bernoulli, the section remains, furthermore, normal to the beam axis after deformation).

In this paper, we studied the static behaviour of FGM beams using the 3D exact beam theory built on 3D Saint-Venant's solution (Ladevèze and Simmonds 1998, El Fatmi and Zenzri 2002), in which the kinematic model includes sectional Poisson's effects and out-of plane warpings. Since it is independent of any kinematic or static assumption. This theory is quite different from the classical theories of Euler-Bernoulli, Timoshenko, and their extensions. This theory is based on a displacement model that allows the deformation of the section in and out of its plane via the main own displacement modes. The latters are specific to the section nature (shape and materials).

2. Functionally graded material

The material properties of FGM beams are assumed to vary continuously through the thickness (see Fig.1). Four homogenization methods exist in literature (Hadji *et al.* 2016, Belabed *et al.* 2014, Pradhan and Chakraverty 2013, Lee and Kim 2013, Ben–Oumrane *et al.* 2009, Zenkour 2006, Zenkour 2007, Ziou *et al.* 2017, Guenfoud 2019) for the computation of Young's modulus $E(y)$ namely: (1) power–law distribution, (2) exponential distribution, (3) Mori–Tanaka scheme and (4) sigmoid distribution.

For the power–law distribution (P–FGM), the Young's modulus is given by (Zenkour 2006, Guenfoud 2019):

$$E(y) = E_b + (E_t - E_b) \times \left(\frac{2y+h}{2h}\right)^P \tag{1}$$

where P is the power–law exponent; E_t and E_b denote the Young's modulus at the top and bottom beam surfaces, respectively.

For the exponential distribution (E–FGM), the Young's modulus is given by (Zenkour 2007, Kaci *et al.* 2014):

$$E(y) = A \times e^{B\times(y+\frac{h}{2})} \quad \text{where } A = E_b \ , \ B = \frac{1}{h} Ln\left(\frac{E_t}{E_b}\right) \tag{2}$$

where h, E_b and E_t denote the thickness of the beam, Young's modulus of the bottom and top faces of beam respectively.

For the Mori–Tanaka distribution (M–FGM), the Young's modulus is given as (Belabed *et al.* 2014)

$$E(y) = E_b + \left(\frac{(E_t - E_b)\times V_c}{1 + (1 - V_c)\times\left(\frac{E_t}{E_b} - 1\right)\times\left(\frac{1+\nu}{3-3\nu}\right)}\right) \tag{3}$$

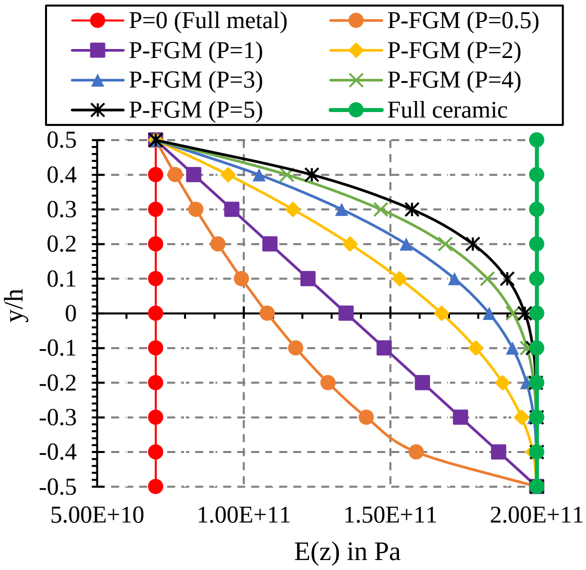

Fig. 2 Variation of Young's modulus through the thickness of P–FGM beam

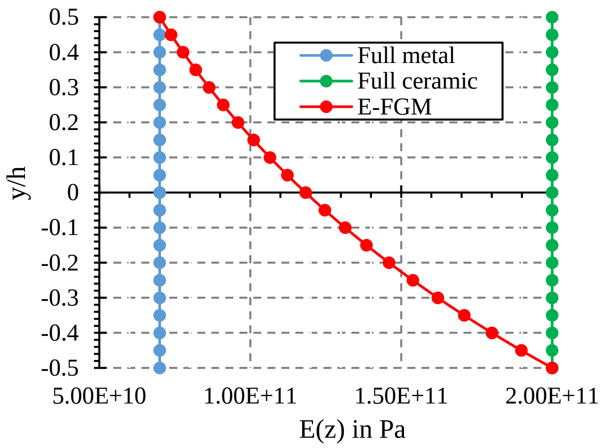

Fig. 3 Variation of Young's modulus through the thickness of E–FGM beam

where $V_c = (0.5 + y/h)^P$ is the volume fraction of the ceramic. Since the effect of the variation of Poisson's ratio ν on the response of FGM beam is insignificant.

At last, the sigmoid distribution (S–FGM) is considered as to reduce the stress concentration in a single power low portion. And then, this type of model is intended to ensure smooth stress distribution using different power–law function as the volume fraction:

$$\begin{cases} V_{c1}(y) = 1 - \dfrac{1}{2}\left(1 - \dfrac{2y}{h}\right)^P & 0 \le y \le \dfrac{h}{2} \\ V_{c2}(y) = \dfrac{1}{2}\left(1 + \dfrac{2y}{h}\right)^P & -\dfrac{h}{2} \le y \le 0 \end{cases} \tag{4}$$

The Young's modulus can be obtained by a linear rule of mixture:

$$\begin{cases} E(y) = E_t V_{c1}(y) + E_b\left(1 - V_{c1}(y)\right); \ 0 \le y \le \dfrac{h}{2} \\ E(y) = E_t V_{c2}(y) + E_b\left(1 - V_{c2}(y)\right); \ -\dfrac{h}{2} \le y \le 0 \end{cases} \tag{5}$$

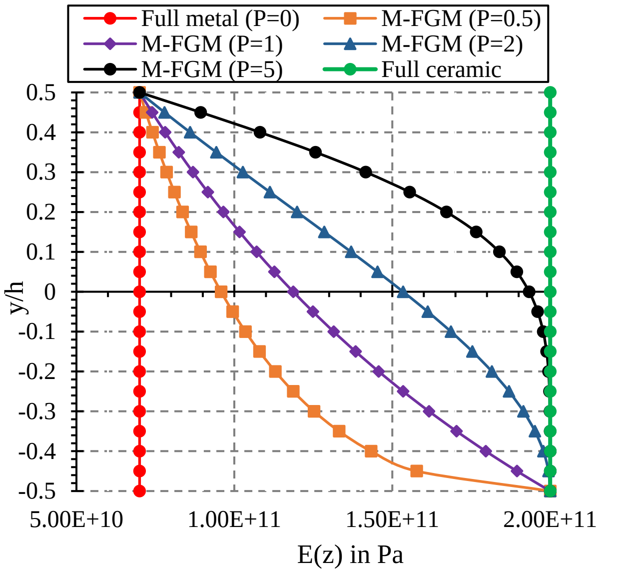

Fig. 4 Variation of Young's modulus through the thickness of M–FGM beam

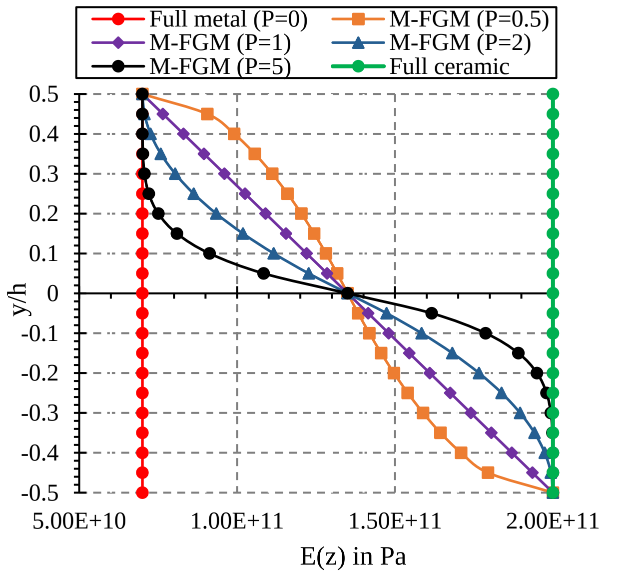

Fig. 5 Variation of Young's modulus through the thickness of S–FGM beam

Figs. 2-5 show the distribution of Young's modulus through the dimensionless thickness of the FGM beam, which is obtained by the different methods (the material properties of this FGM beam are presented in Section 5).

Many studies (Delale and Erdogan 1983, Ben–Oumrane *et al.* 2009, Guenfoud *et al.* 2016, Hadji *et al.* 2016, Ziou 2017) indicated that the effect of Poisson's ratio on the deformation is much less than the Young's modulus. Therefore, in this paper, the Poisson's ration is assumed to be a constant.

3. Saint Venant beam theory

We consider the beam shown in Fig. 6, occupying a prismatic domain Ω of a constant cress-section S and a

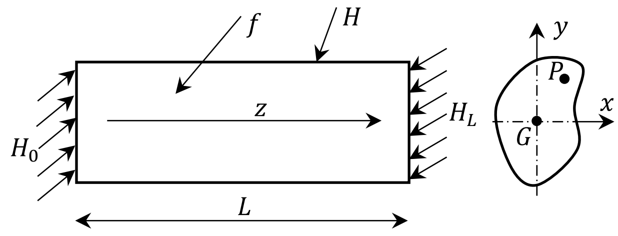

Fig. 6 Geometry and loading on the beam (3D)

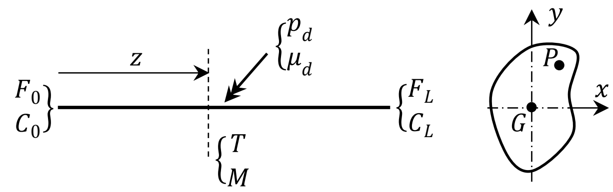

Fig. 7 Actions on the beam (1D)

length L. The beam is subjected to a body force density f on Ω, a surface force density H on the lateral surface S_{lat}, a surface force density H_0 on S_0 and a surface force density H_L on S_L. Where S_0 and S_L denote the cross-section at $z = 0$ and the cross-section at $z = L$, respectively. A point P in Ω is marked $P = zn(z) + X$, where X belongs to S. The materials constituting the beam are linear elastic and the elastic tensor K is z –constant.

The 3D elasticity problem to be solved can then be written (Ladevèze and Simmonds 1998, El Fatmi and Zenzri 2002):

Equilibrium equations

Equilibrium equations of this problem can be written:

$$div\sigma + f = 0 \quad on\,\Omega \tag{6}$$

$$\sigma n(x,y,z) = H \quad on\, S_{lat} \tag{7}$$

$$\sigma n(z) = H_L \quad on\, S_L \tag{8}$$

$$-\sigma n(z) = H_0 \quad on\, S_0 \tag{9}$$

Constitutive relation

The constitutive relation is

$$\sigma = K\varepsilon(U) \quad on\,\Omega \tag{10}$$

where

$$\varepsilon(U) = \tfrac{1}{2}(\nabla^t U + \nabla U) \quad on\,\Omega \tag{11}$$

where U is the displacement vector, σ is the stress, K is Hooke's tensor, ε the strain tensor, $n(x,y,z)$ is unit normal and external to the boundary of domain Ω and $n(z)$ is unit normal and external to cross-section of the z–abscissa.

The resultant T and the moment M in the cross-section of the stress vector $\sigma.n(z)$ are classically named "generalized stresses" or "cross-sectional stress resultants", they are defined by:

$$T(z) = \int_S \sigma(n(z))ds = \begin{Bmatrix} T_x \\ T_y \\ N \end{Bmatrix} \tag{12}$$

$$M(z) = \int_S X \wedge \sigma(n(z))ds = \begin{Bmatrix} M_x \\ M_y \\ M_t \end{Bmatrix} \tag{13}$$

where the components $\{T_x, T_y, N, M_x, M_y, M_t\}$ are the six classical internal forces designated respectively by the shear forces, the normal force, the bending moments and the torsional moment.
which verify the one–dimensional (1D) equilibrium equations:

$$\begin{cases} T_{,z} + p_d = 0 \\ M_{,z} + n(z) \wedge T + \mu_d = 0 \end{cases} \tag{14}$$

where $(\cdot)_{,z}$ is the derivative with respect to z. p_d, μ_d are the linearized force densities associated with f, H (Fig.7).

$$p_d = \int_S f dS + \int_{\partial S} H d\tau \tag{15}$$

$$\mu_d = \int_S X \wedge f dS + \int_{\partial S} X \wedge H d\tau \tag{16}$$

The one–dimensional (1D) behaviour law of the beam is given by:

$$\begin{Bmatrix} T \\ M \end{Bmatrix} = \Gamma \begin{Bmatrix} u' + n(z) \wedge \omega \\ \omega' \end{Bmatrix} \tag{17}$$

and

$$\begin{Bmatrix} \gamma \\ \chi \end{Bmatrix} = \begin{Bmatrix} u' + n(z) \wedge \omega \\ \omega' \end{Bmatrix} = \Lambda \begin{Bmatrix} T \\ M \end{Bmatrix} \tag{18}$$

where Γ is the sectional stiffness operator (matrix 6×6) depending on the cross–section and the materials. We note $\Lambda = \Gamma^{-1}$ the flexibility operator (compliance operator).

The equilibrium Eq. (14) and the behaviour law Eq. (18) constitute the differential equations of the exact 1D beam theory. In order to be solved, the 1D problem has to be completed by boundary conditions (Ladevèze and Simmonds 1998, El Fatmi and Zenzri 2002, El Fatmi and Zenzri 2004).

Three-dimensional Saint–Venant's solution

The Saint–Venant solution, denoted by (σ^{SV}, U^{SV}), is the single z–polynomial solution that exactly satisfies Eqs. (6)-(7)-(10)-(11) and satisfies the boundary conditions of Eqs. (8)-(9) only in terms of resultant (force and moment) of the stresses applied on the extremity cross-sections.

The 3D Saint–Venant's solution is given as following (Ladevèze and Simmmonds 1998, El Fatmi and Zenzri 2002, El Fatmi and Zenzri 2004, El Fatmi 2016):

The 3D stress field in a cross-section is obtained by:

$$\sigma^e(x,y,z) = T_x^e(z).\sigma^1(x,y) + T_y^e(z).\sigma^2(x,y) + N^e(z).\sigma^3(x,y) + M_x^e(z).\sigma^4(x,y) + M_y^e(z).\sigma^5(x,y) + M_t^e(z).\sigma^6(x,y) \tag{21}$$

or in a compact form

$$\sigma^e(x,y,z) = \sum_{i=1}^{6} X_i^e(z)\sigma^i(x,y) \tag{22}$$

where:

$X_i^e(z)$ symbolizes the six (06) internal forces: $T_x^e(z), T_y^e(z), T_z^e(z), M_x^e(z), M_y^e(z), M_t^e(z)$.

They obtained from the one-dimensional (1D) equilibrium equations.

$\sigma^i(x,y)$ is the section stress field that correspond to each of the unit internal forces $X_i^e = 1$ (unity). The six (06) unit stress fields $\sigma^i(x,y)$ are depend only on the section nature (shape and materials), they are characteristics of the section (El Fatmi and Zenzri 2002).

The expression of the displacement field derives from Saint Venant's 3D solution, is given by:

$$U^{SV}(x,y,z) = u^e(z) + \omega^e(z) \wedge X + T_x^e(z).U^1(x,y) + T_y^e(z).U^2(x,y) + N^e(z).U^3(x,y) + M_x^e(z).U^4(x,y) + M_y^e(z).U^5(x,y) + M_t^e(z).U^6(x,y) \tag{23}$$

or in a compact form

$$U^{SV}(x,y,z) = \overbrace{u^e(z) + \omega^e(z) \wedge X}^{rigid\ motion\ of\ the\ section} + \overbrace{\sum_{i=1}^{6} X_i^e(z)U^i(x,y)}^{Sectional\ strain} \tag{24}$$

where

$u(z)$ and $\omega(z)$ are the sectional translation and rotation vector respectively, are related to (T, M) by the one–dimensional structural behaviour of Eq. (18).

$U^i(x,y)$ are the six (06) sectional displacement modes of 3D Saint–Venant that correspond to each of the unit internal forces $X_i^e = 1$ (unity). Each one of the six 3D Saint–Venant modes $U^i(x,y)$ reflects the contribution of an internal force to the sectional deformation, describing Poisson's effects (deformation in the plane of the section) and that out–of plane warpings. The six sectional displacement modes $U^i(x,y)$ depend only on the section nature (shape and materials); they are sectional characteristics.

The first term of the Eq. (24) represents global motion of the section, and the second term expresses the section deformation.

4. Mechanical characteristics of the section

4.1 Homogeneous and isotropic section

Structural flexibility operator

The structural flexibility operator Γ (matrix 6×6) is depends only on the cross-section nature (shape and the material), it is used to describe the one-dimensional (1D) behaviour of beam (see Eq. (18)). For the case of homogeneous and isotopic section, the structural flexibility operator is given by

$$\Lambda = \begin{bmatrix} \frac{1}{GS_x}+\frac{y_c^2}{GJ} & \frac{-x_c y_c}{GJ} & 0 & 0 & 0 & \frac{y_c}{GJ} \\ \frac{-x_c y_c}{GJ} & \frac{1}{GS_y}+\frac{x_c^2}{GJ} & 0 & 0 & 0 & \frac{-x_c}{GJ} \\ 0 & 0 & \frac{1}{ES} & 0 & 0 & 0 \\ 0 & 0 & 0 & \frac{1}{EI_x} & 0 & 0 \\ 0 & 0 & 0 & 0 & \frac{1}{EI_y} & 0 \\ \frac{y_c}{GJ} & \frac{-x_c}{GJ} & 0 & 0 & 0 & \frac{1}{GJ} \end{bmatrix} \quad (25)$$

Where E is the Young's modulus, G is the shear modulus, S the cross-section, S_x and S_y are the reduced sections related to the shear forces T_x and T_y respectively, I_x the inertia moment with respect to x, I_y the inertia moment with respect to y, J the torsional inertia, x_c and y_c are the coordinates of the shear centre C.

3D stress field

For the case of a homogeneous and isotropic section, the stress field $\sigma^e(x,y,z)$ is given, in (x,y,z), by

$$\sigma^e(x,y,z) = \begin{bmatrix} 0 & 0 & \sigma_{xz}^e \\ 0 & 0 & \sigma_{yz}^e \\ \sigma_{xz}^e & \sigma_{yz}^e & \sigma_{zz}^e \end{bmatrix} \quad (26)$$

The axial stress σ_{zz}^e depends only on (N^e, M_x^e, M_y^e) and the shear stresses $(\sigma_{xz}^e, \sigma_{yz}^e)$ depend only on (T_x^e, T_y^e, M_t^e).

Axial stress which is linear combination of (N^e, M_x^e, M_y^e) is given by

$$\sigma_{zz}^e(x,y,z) = N^e(z).\left(\frac{1}{A}\right) + M_x^e(z).\left(\frac{y}{I_x}\right) - M_y^e(z).\left(\frac{x}{I_y}\right) \quad (27)$$

We can deduce the stress fields σ^i associated with (N^e, M_x^e, M_y^e) and which reduce to the axial stress by:

$$\sigma^3(x,y) = \begin{bmatrix} 0 & 0 & 0 \\ 0 & 0 & 0 \\ 0 & 0 & \frac{1}{A} \end{bmatrix}$$
$$\sigma^4(x,y) = \begin{bmatrix} 0 & 0 & 0 \\ 0 & 0 & 0 \\ 0 & 0 & \frac{y}{I_x} \end{bmatrix} \quad (28)$$
$$\sigma^5(x,y) = \begin{bmatrix} 0 & 0 & 0 \\ 0 & 0 & 0 \\ 0 & 0 & -\frac{x}{I_y} \end{bmatrix}$$

These fields depend only on (A, I_x, I_y), they are specific on the section.

Shear stresses which are linear combination of (T_x^e, T_y^e, M_t^e) are written:

$$\begin{aligned} \sigma_{xz}^e(x,y,z) &= f_x^x(x,y).T_x^e(z) + f_x^y(x,y).T_y^e(z) + f_x^t(x,y).M_t^e(z) \\ \sigma_{yz}^e(x,y,z) &= f_y^x(x,y).T_x^e(z) + f_y^y(x,y).T_y^e(z) + f_y^t(x,y).M_t^e(z) \end{aligned} \quad (29)$$

where the functions $f_x^x(x,y)$, $f_x^y(x,y)$, $f_x^t(x,y)$, $f_y^x(x,y)$, $f_y^y(x,y)$ and $f_y^t(x,y)$ depend on the section nature (shape and material) and which, they can only be determined numerically (with the exception of the circular section for which these functions can be determined analytically).

3D displacement field

The $U^i(x,y)$ fields that express the strains of the section can be decomposed into a strain in the section plane (Poisson's effects) and an out–of–plane strain (warping). For the case of a homogeneous and isotropic section, we can note that:

Normal effort and the bending moments (N, M_x, M_y) only lead to Poisson's effects: $[U^3(x,y), U^4(x,y), U^5(x,y)]$ so are plans (their component with respect to z is zero).

Shear forces and torsional moments (T_x, T_y, M_t) only lead to warping: $[U^1(x,y), U^2(x,y), U^6(x,y)]$ so are out–of plane (their components with respect to x and y are zero).

4.2 Composite section

For composite section where each material can be anisotropic, the 1D behaviour of Eq. (18) can be described by a full (6×6) matrix, and several elastic coupling can occur between extension, bending and torsion. These are due to several factors such as the non symmetry of the section, the position of each material and the anisotropy of the materials.

For a composite section, we denote, by analogy to the homogeneous case, the stiffness constants as follows:

$\widetilde{GS}_x$ the shear force stiffness $/x$

$\widetilde{GS}_y$ the shear force stiffness $/y$

$\widetilde{ES}$ the axial stiffness

$\widetilde{EI}_x$ the bending stiffness $/x$

$\widetilde{EI}_y$ the bending stiffness $/y$

$\widetilde{GJ}$ the torsional stiffness.

3D stress field

For the case of a homogeneous and isotropic section, the components σ_{xx}, σ_{yy} and σ_{xy} of the stress field were null (Eq. (26)), but these components are not zero for the case of any composite section (see Eq. (30)).

It is sufficient, for example, that the Poisson's effects are different from one material to another so that it generates stresses in the plane of the section, around the interfaces between the materials (supposed perfectly adherent)

$$\sigma^e(x,y,z) = \begin{bmatrix} \sigma_{xx}^e & \sigma_{xy}^e & \sigma_{xz}^e \\ \sigma_{xy}^e & \sigma_{yy}^e & \sigma_{yz}^e \\ \sigma_{xz}^e & \sigma_{yz}^e & \sigma_{zz}^e \end{bmatrix} \quad (30)$$

3D displacement field

In contrast with the case of homogeneous and isotropic section, each cross-sectional stress $(T_x, T_y, N, M_x, M_y, M_t)$ contributes to the Poisson's effect deformation and to the out–of–plan warping of the section, this is due to the composite nature of the section (El Fatmi 2012).

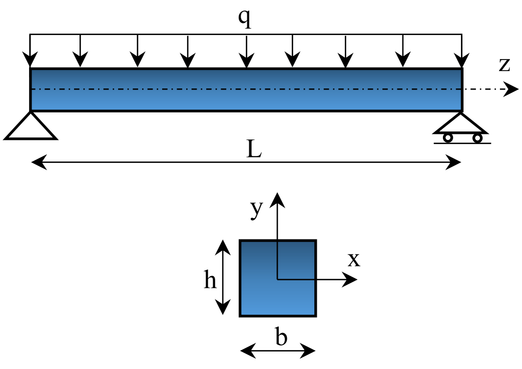

Fig. 8 Simply supported FGM beam

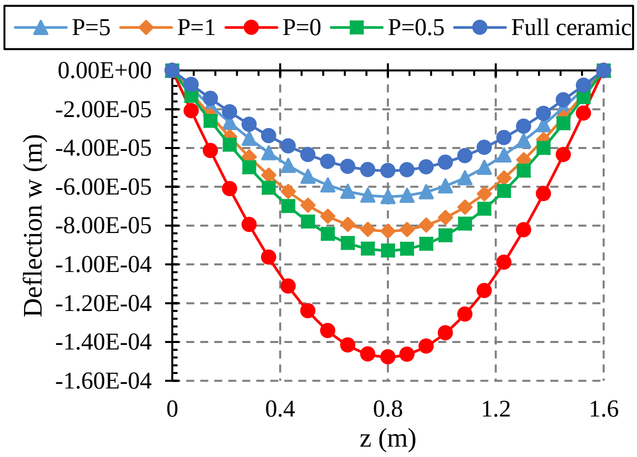

Fig. 10 Deflection along the length of the beam obtained by Saint-Venant theory.

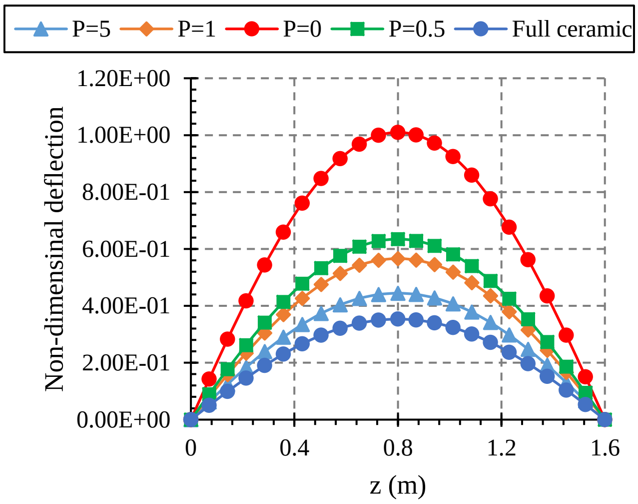

Fig. 11 Non-dimensional deflection along the length of the beam obtained by Saint-Venant theory.

5. Application

In this section, we study a simply supported FGM beam ($L = 1.6m, h = 0.10m, b = 0.10m$) subjected to a uniformly distributed load q (Fig. 8). The beam is composed of Zirconia ($Zro2{:}\, E_c = 200\, GPa, \nu = 0.30$) and aluminium ($AL{:}\, E_m = 70\, GPa, \nu = 0.30$); its properties varied through the thickness of the beam according to various methods presented in Section 2 (see Figs. 2-5). The bottom surface of the beam ($y = -h/2$) is pure Zirconia, whereas the top surface of the beam ($y = +h/2$) is pure Aluminum.

Şimşek (2009) and Ziou (2017) studied the same FGM beam by Timoshenko and the higher order shear deformation beam theories. They assumed that the properties of this beam are varied according to power-law. A comparison between our results and those obtained by Şimşek (2009) and Ziou (2017) is present in this Section.

5.1 Numerical tool

The Matlab tool CSB, developed by El Fatmi and Zenzri (2002), is used in this work in order to study the behaviour of an FGM using the 3D Saint-Venant theory.

CSB is a package of two complementary numerical tools named CSection and CBeam. For a given beam problem, Csection ensures the cross-section analysis by 2D–FEM to provide the set of sectional modes ($U^i(x, y)$) which are then used by Cbeam to solve the beam problem by 1D FEM according to the displacement model.

5.2 Modelling and results

5.2.1 Modelling of the P-FGM

In the work, we modelled the P-FGM beam using the 3D Saint Venant's beam theory. The materials properties of this beam are assumed that vary according to the power-law distribution. Fig. 2 (Section 2) shows the variation of Young's modulus (modulus of elasticity) through the beam dimensionless thickness for various values of the power-law index P. For P = 0 and P = +∞, the beam corresponds to the isotropic metal and ceramic, respectively, whereas the composition of metal and ceramic is linear for P = 1.

Delale and Erdogan (1983) indicated that the effect of Poisson's ratio on the deformation is much less than that of Young's modulus. Thus, Poisson's ratio of the beams is assumed to be constant and is chosen to be 0.3.

Figs. 10 and 11 show the deflection (w) and the non-dimensional deflection (w/w_{static}) of the FGM beam respectively. The static deflection of the fully aluminum beam under the uniformly distributed load is computed by:

$$w_{static} = \frac{5 \times q \times L^4}{384 \times E_m \times I} \tag{31}$$

We see that the deflection of full metal (P = 0) is greater than that of full ceramic (P = +∞), this can be accounted for Young's modulus of ceramic being higher than that of metal. The FGM beam deflection (P ≠ 0) is between those of beams made of ceramic and metal. Hence, for the FGM beam, transverse deflection decreases as the power-law exponent P is increased. This is due to the fact an increase in the power-law exponent yields a decrease in the bending rigidity of the beam.

Table 1 Non-dimensional deflection at mid–span of the FGM beam

	Present work		Şimşek (2009)		Ziou (2017)	
P	SVBT(1)	RBT(2)	TBT(3)	HOSDT(4)	TBT(3)	CBT(5)
P = 0	1.00980	1.00816	1.00812	1.00975	1.00976	1.00001
P = 0.5	0.63453	0.63317	0.63953	0.64065	/	/
P = 1	0.56612	0.56490	0.56615	0.56699	0.56585	0.56180
P = 5	0.44441	0.44355	0.44391	0.44442	0.4451	0.44069
P = ∞	0.35343	-	0.35284	0.35341	0.35341	0.35000

(1) SVBT: Saint-Venant beam theory, (2) RBT: Refined Beam theory, (3)TBT: Timoshenko beam theory, (4)HOSDT: Higher order shear deformation theory, (5)CBT: Euler-Bernoulli theory.

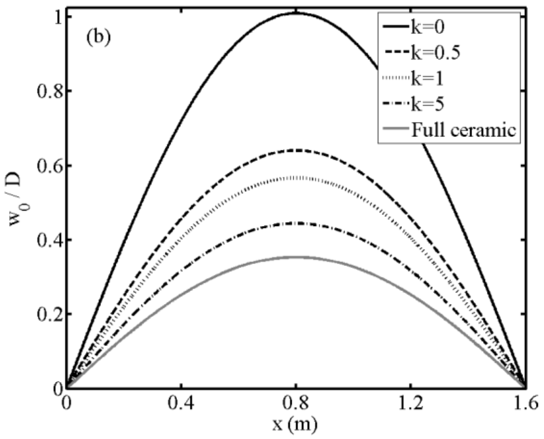

Fig. 12 Non-dimensional deflection along the length of the beam (Şimşek 2009)

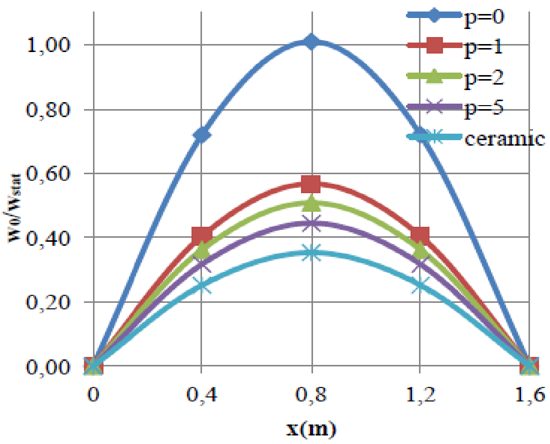

Fig. 13 Non-dimensional deflection along the length of the beam (Ziou 2017)

The non-dimensional deflections (Fig. 11), obtained by the Saint-Venant's solution, are compared with those provided by Şimşek (2009) and Ziou (2017) using the higher order shear deformation and Timoshniko theories (see Figs. 12 and 13). It is observed that the results obtained by the three models are identical.

Table 1 shows also a comparison of the non-dimensional deflections at mid-span of the FGM beam obtained using the theories proposed here with those given by Şimşek (2009) and Ziou (2017). It is seen that the non-dimensional deflections obtained with SVBT and RBT are very close to those obtained by TBT, HOSDT and CBT.

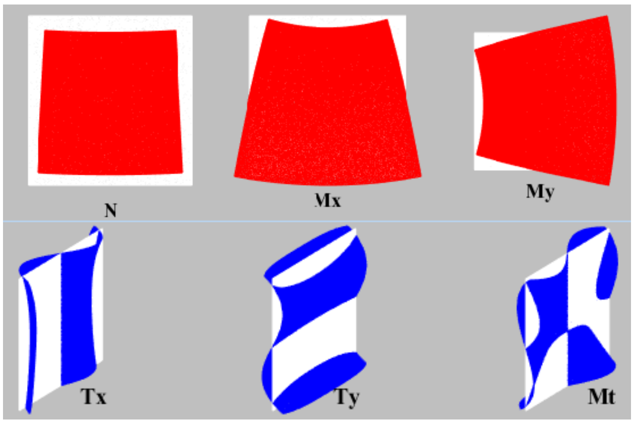

Fig. 14 Saint-Venant sectional modes (Poisson's effects and out-of plane Warpings) for the case of FGM beam with P=5

Fig. 14 shows the six (06) Saint-Venant's sectional modes related to the six classical internal forces $(T_x, T_y, N, M_x, M_y, M_t)$: the three modes in red colour are related to the Poisson's effects due to the axial force (N) and the bending moments (M_x, M_y), whereas the three modes in blue colour are related to the out-of plane warpings due to the shear forces (T_x, T_y) and the torsional moment (M_t). The six modes presented in Fig. 14 are given only for the case of FGM beam with P = 5. We note that these modes are specific only to the section nature (shape and materials).

Fig.15 show the 3D Saint-Venant's sectional stress field at mid-span of the beam for the two cases: firstly in the homogeneous cross-section in which P = 0 (Fig. 15(a)) and secondly in the FGM beam with P = 5 (Fig. 15(b)). We can see that the 3D stress distribution, for the homogeneous section (full metal), describes an inclined plane shape passes to the middle axis of the section (x-axis), as shown in Fig. 15(a). However the shape of the 3D stress distribution, for the FGM beam case with P = 5, is not plane and does not pass to the middle axis of the section (x-axis)), as shown in Fig. 15(b).

Fig. 16 shows the axial stress distribution through the thickness at the mid-span of FGM beam for various values of P. We can see that axial stress distribution is linear only for the full metal (P = 0), but for the other cases ($P \neq 0$) the axial stress distribution is not linear, and also the tensile stress values are greater than compressive stresses in FGM beam. We noted also that for full metal, the axial stress value is zero ($\sigma_{zz} = 0$) at the mid-plane ($h/y = 0$) but it is clearly visible that for the other cases ($P \neq 0$) the axial stresses values at the mid-plane of FGM beam are not zero. This indicates that the neutral plane of the beam moves towards the lower side of the FG beam. This is due to the variation of the modulus of elasticity through the thickness of the FGM beam.

The axial stresses, σ_{zz}, are computed at the mid-span of the beam (Figs. 15 and 16), and the shear stresses, τ, are evaluated at the support of the beam (Figs.19-20-21-22-23-25).

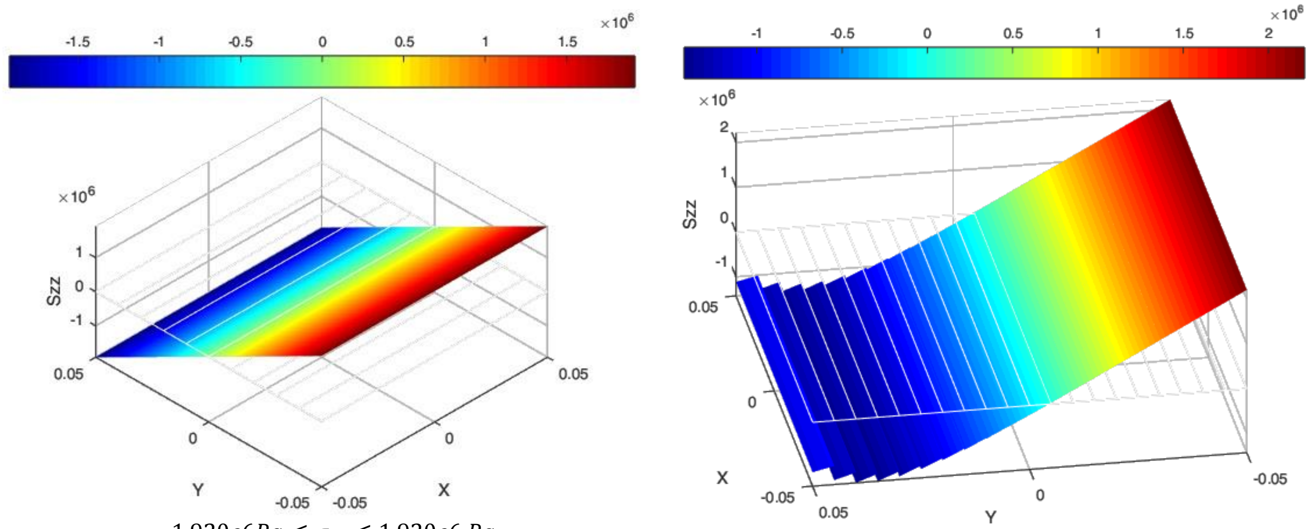

$-1.920e6Pa \leq \sigma_{zz} \leq 1.920e6\ Pa$ $-1.505e6Pa \leq \sigma_{zz} \leq 2.205e6\ Pa$

(a) Axial stress distributions obtained by SVBT (P=0) (b) Axial stress distributions obtained by SVBT (P=5)

Fig. 15 Axial stress distributions obtained by SVBT (P = 0) and (P = 5)

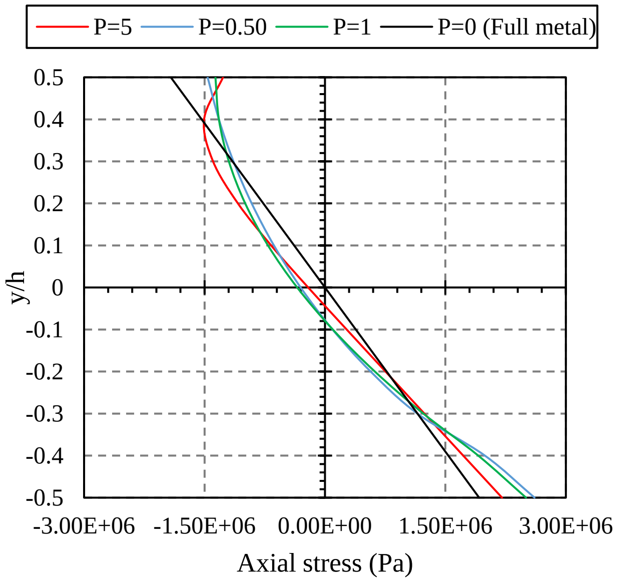

Fig. 16 Axial stress distributions obtained by SVBT at $x = -b/2$

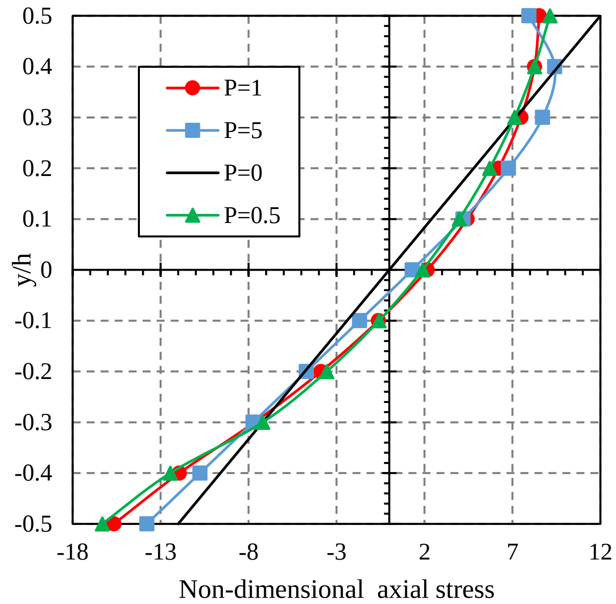

Fig. 17 Non-dimensional axial stress distributions at $x = -b/2$

The axial and shear stresses are normalized by

$$\overline{\sigma_{ZZ}} = \frac{\sigma_{zz} \times b \times h}{q \times L}$$
$$\overline{\tau_{Zy}} = \frac{\tau_{zy} \times b \times h}{q \times L} \tag{32}$$

Non-dimensional axial stresses, $\overline{\sigma_{zz}}$, obtained by Saint-Venant's beam theory from Eq. (32), are compared with these extracted from the works of Şimşek (2009) and Ziou (2017) (see Fig. 18). It can observed that, the results obtained by our investigation (Fig. 17) are in very good agreement with these of other investigations shown in Fig. 18.

The 3D shear stress fields, $\tau = \sqrt{(\tau_{zx})^2 + (\tau_{zy})^2}$, obtained by Saint-Venant theory for various values of the power-law index P are illustrated in Figs. 19-20-21-22.

Figs. 23 and 25 show the distribution of the shear stress through the thickness of the beam at $x = -b/2$ and $x = 0$, respectively, their corresponding non-dimensional shear stress are presented in the Figs. 24 and 26. The latter are compared with those obtained by Şimşek (2009) and Ziou (2017). This comparison demonstrates that our results (Fig. 26) are identical to those obtained by Şimşek (2009) using the higher order shear deformation theory (Fig.27(a)) and, on other hand to those obtained by Ziou (2017) using Timoshniko theory (Fig.27(b)).

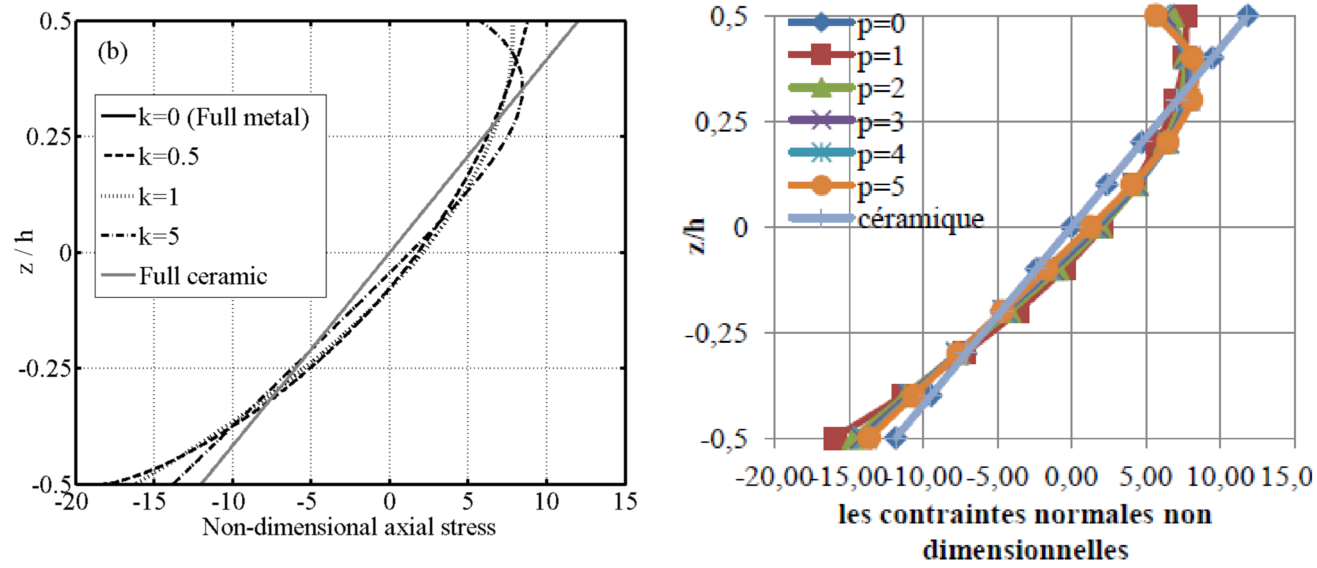

(a) Non-dimensional axial stress distributions (Şimşek 2009) (b) Non-dimensional axial stress distributions (Ziou 2017)

Fig. 18 Non-dimensional axial stress distributions provided by Şimşek (2009) and Ziou (2017)

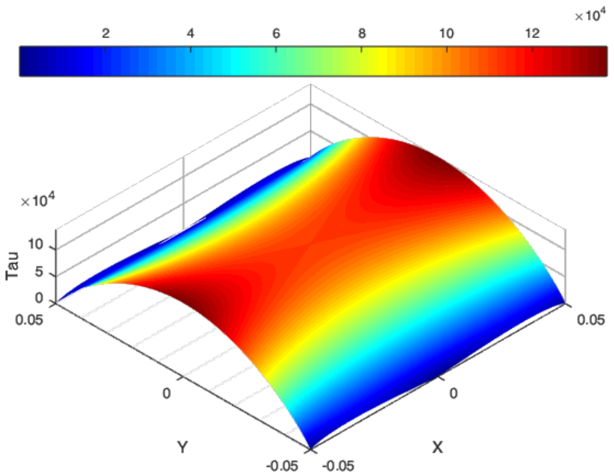

$4.820Pa \leq \tau \leq 1.375e5\ Pa$

Fig. 19 Shear stress distributions obtained by SVBT (P=0)

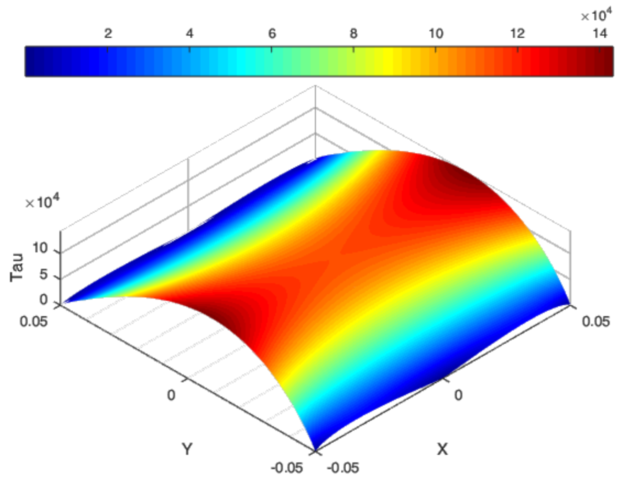

$2.950Pa \leq \tau \leq 1.433e5\ Pa$

Fig. 21 Shear stress distributions obtained by SVBT (P=1)

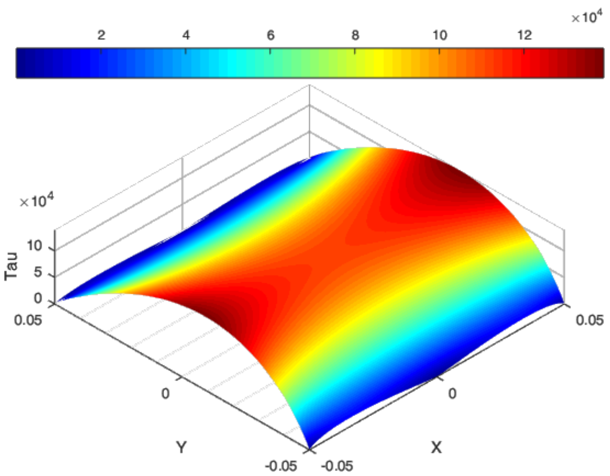

$3.169Pa \leq \tau \leq 1.388e5\ Pa$

Fig. 20 Shear stress distributions obtained by SVBT (P=0.5)

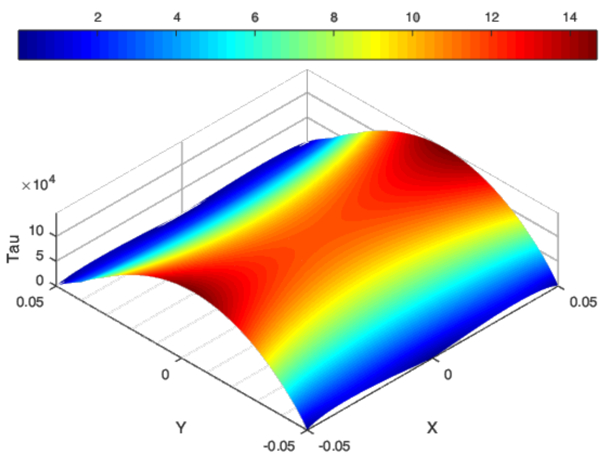

$2.926Pa \leq \tau \leq 1.468e5\ Pa$

Fig. 22 Shear stress distributions obtained by SVBT (P =5)

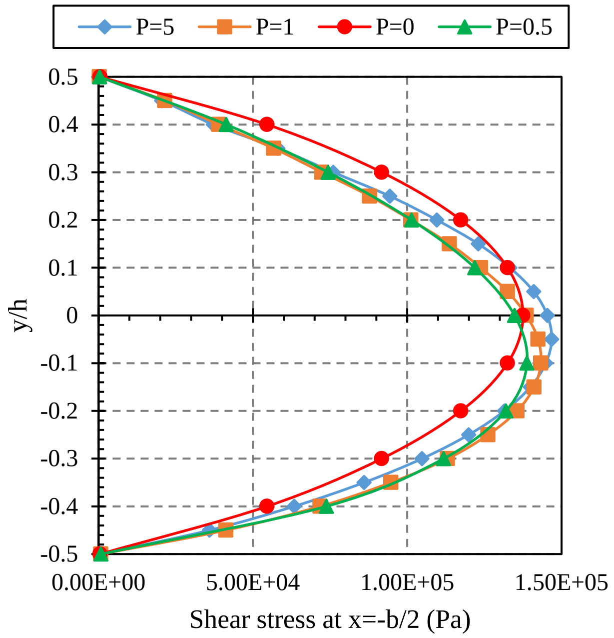

Fig. 23 Shear stress distributions at $x = -b/2$

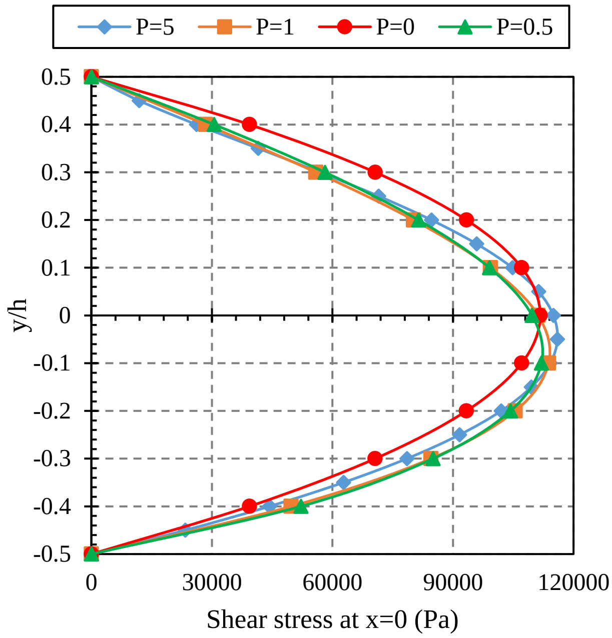

Fig. 25 Shear stress distributions at $x = 0$

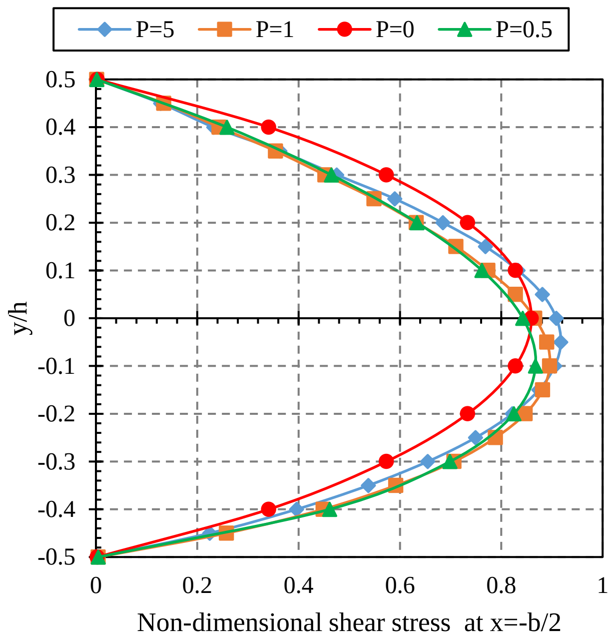

Fig. 24 Non–dimensional shear stress distributions at $x = -b/2$

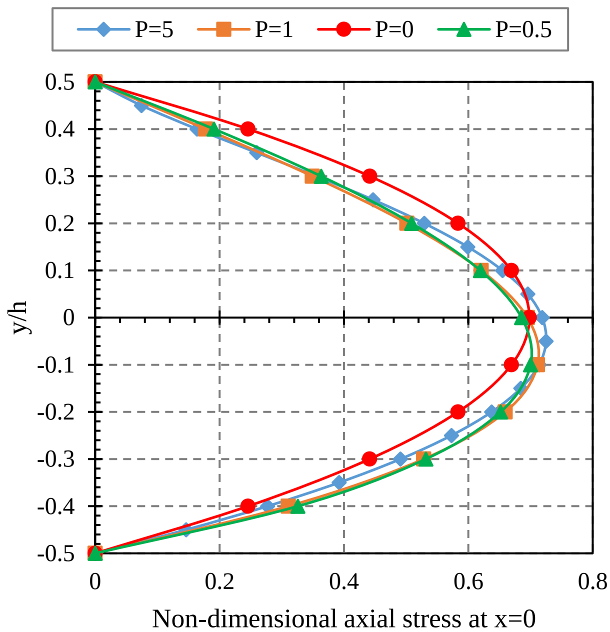

Fig. 26 Non–dimensional shear stress distributions at $x = 0$

It is to be noted that the maximum value of the shear stress is occurs at $y/h = -0.1$ for the cases of P = 0.5 and P = 1. Whereas for the case of P = 5, the maximum value of τ is occurs at y/h = -0.05, not at the beam center as in the homogeneous case (shear stress is maximum on the neural axis of the homogeneous beam).

Fig. 28 shows a comparison of the shear stress distribution through the thickness at $x = -b/2$ and $x = 0$ (for the case of P = 5). It can see that the shear stress at $x = -b/2$ (distribution through the extremity of the section) is greater that the shear stress at $x = 0$ (distribution through the central axis of the section).

In the following part of this work, we study the behaviour of the same beam (Fig.8), but in this time, we consider a various material beams such as E-FGM, S-FGM and M-FGM beams. We present also a comparison between, on one hand, the results obtained for these beams and, on the other hand, the results of the P-FGM beam.

5.2.2 Modelling of the E-FGM beam

We will now study the behaviour of the previous beam,

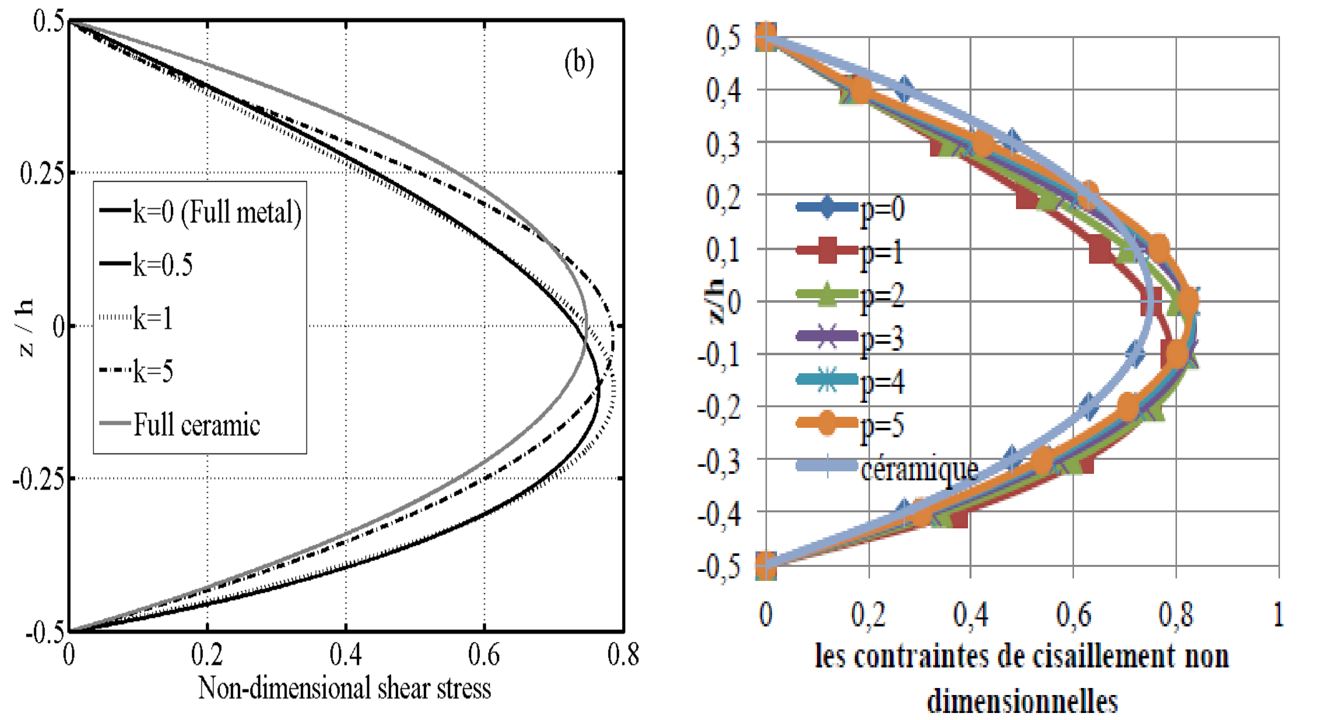

(a) Non–dimensional shear stress distributions (Şimşek 2009) (b) Non–dimensional shear stress distributions (Ziou 2017)

Fig. 27 Non–dimensional shear stress distributions provided by Şimşek (2009) and Ziou (2017)

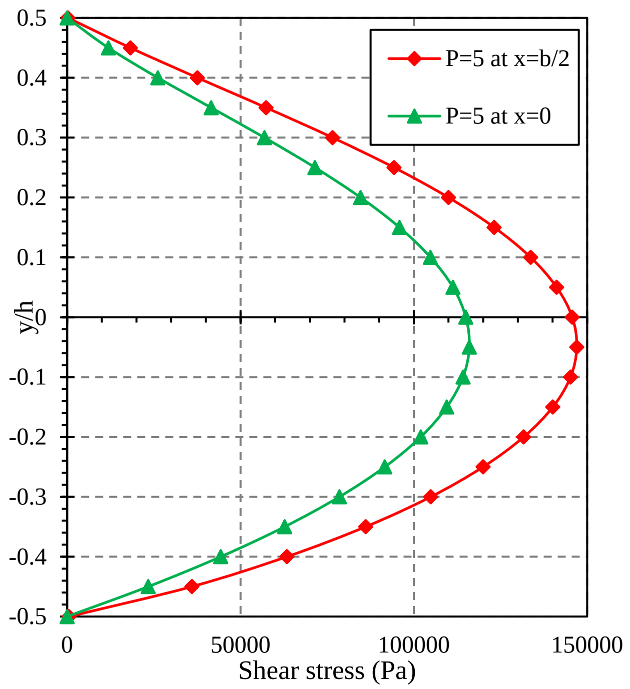

Fig. 28 Shear stress distributions

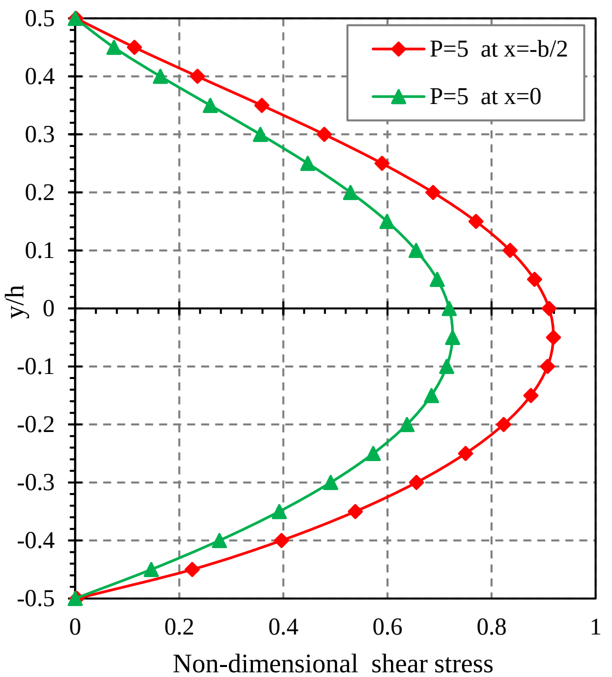

Fig. 29 Non–dimensional shear stress distributions

but this time we consider that the material properties of FGM beams are vary continuously through the thickness according to the exponential distribution method (E-FGM). Fig. 3 (Section 2) shows the variation of Young's modulus through the beam dimensionless thickness. It can be observed that this variation is not linear.

E-FGM deflection obtained by the Saint-Venant solution is shown in the Fig. 30. This deflection is compared with the P-FGM beam deflections (for various values of P). We can observed that the non-dimensional deflection at mid-span of E-FGM beam is close to that of P-FGM beam when P = 0.5 (see also Table. 2).

The axial stress field, obtained by 3D Saint–Venant's solution, is shown in Fig. 31. The shape of this 3D stress distribution, is not plane and does not pass to the middle axis of cross-section (x-axis) as shown in Fig. 32. In order

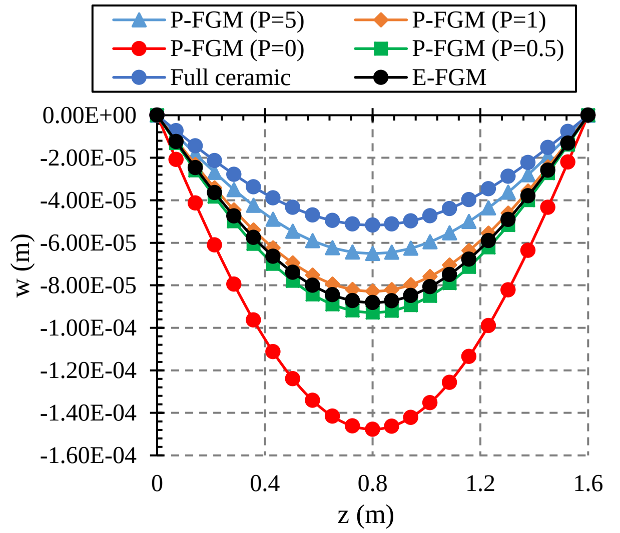

Fig. 30 Comparison between P-FGM and E-FGM deflections obtained by Saint-Venant theory.

Table 2 Comparison of the non-dimensional deflection values at mid-span of various FGM beams

P	P-FGM	E-FGM	S-FGM	M-FGM
P = 0	1.00980		1.00980	1.00980
P = 0.5	0.63453		0.54491	0.67962
P = 1	0.56612	0.60244	0.56671	0.60135
P = 5	0.44441		0.62011	0.46655
P = ∞	0.35343		0.35343	0.35343

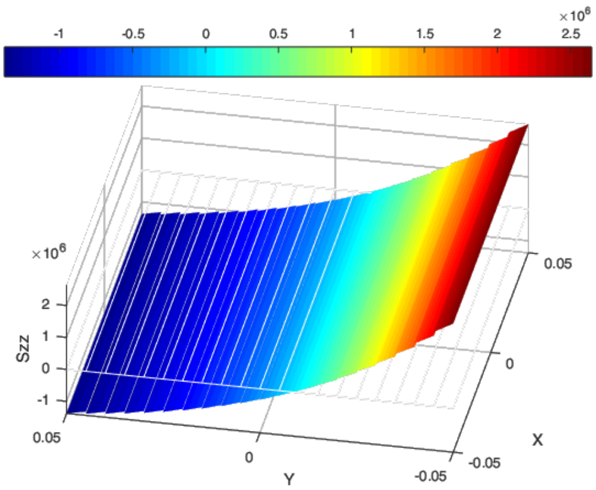

$-1.378e6Pa \leq \sigma_{zz} \leq 2.645e6\ Pa$

Fig. 31 Axial stress distribution of E-FGM beam

to compare the results of E-FGM beam and those of P-FGM beams, we consider an axial stress distribution through y-axis passes by the abscissa $x = 0$ (see Fig. 32 and Table. 3). We see that the axial stress of E-FGM is close to that of P-FGM when $P = 0.5$ and $P = 1$.

The 3D shear stress field of E-FGM beam is plotted in Fig. 33. It is to be noted that the maximum value is occurs at $y/h = -0.1$ (Fig 34), whereas the shear stress of the homogeneous case is symmetric about the mid-plane of the beam.

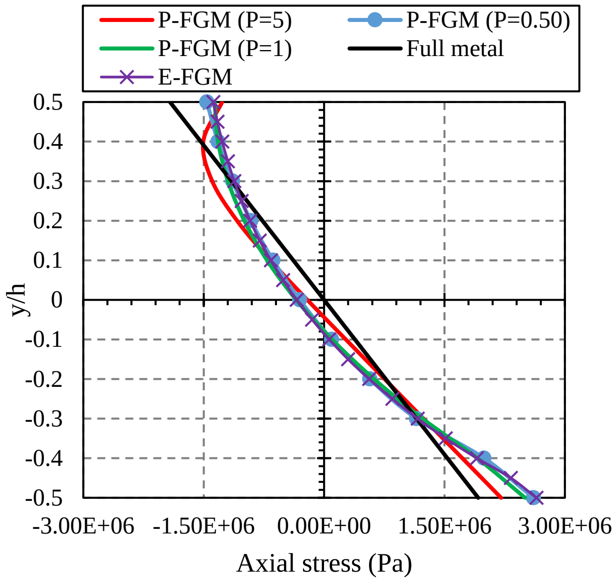

Fig. 32 Axial stress distributions obtained by SVBT

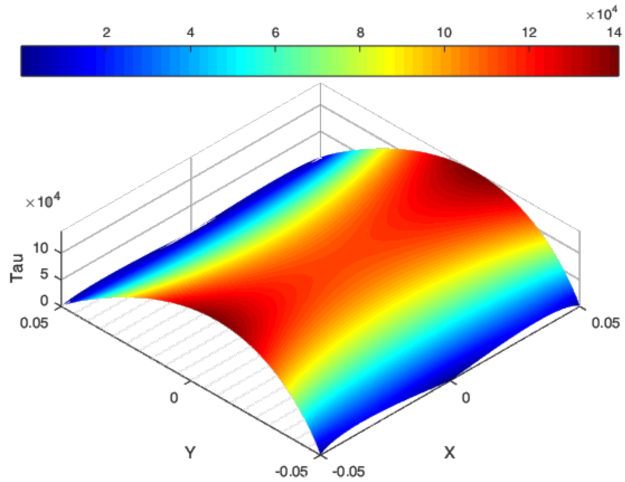

$7.681Pa \leq \tau \leq 1.411e5\ Pa$

Fig. 33 Shear stress distribution of E-FGM beam

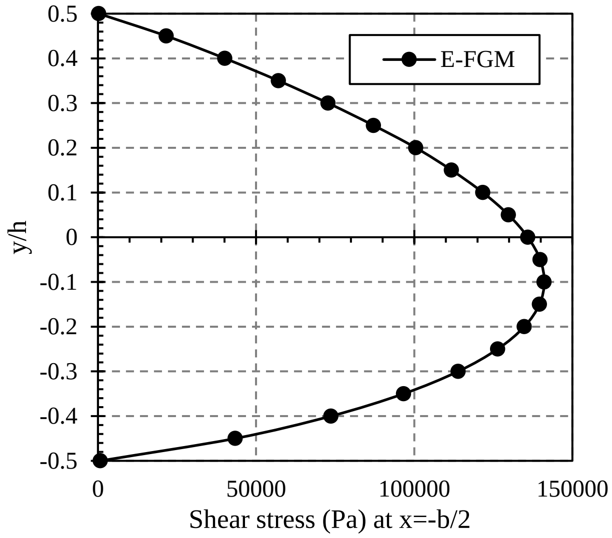

Fig. 34 Shear stress distributions at $x = -b/2$ of E-FGM beam

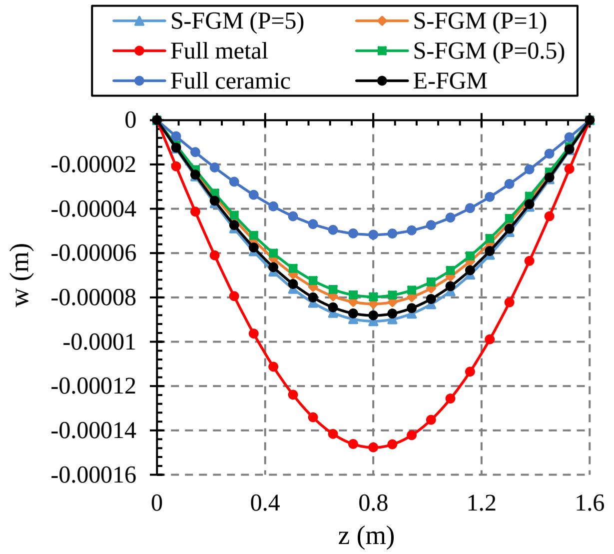

Fig. 35 Comparison between S-FGM and E-FGM deflections obtained by Saint-Venant's theory.

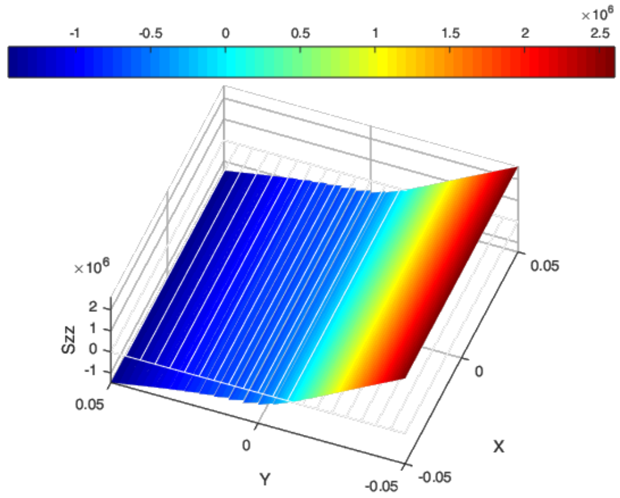

$-1.450e6Pa \le \sigma_{zz} \le 2.602e6\ Pa$
Fig. 36 Axial stress distribution of S-FGM beam (P = 5)

5.2.3 Modelling of the S-FGM beam

We study also the behaviour of same beam, in this time, the material properties of FGM beams are assumed to vary continuously through the thickness according to the sigmoid distribution method (S-FGM), the variation of Young's modulus through the beam dimensionless thickness is depicted in Fig. 5 (Section 2).

Fig. 35 shows the S-FGM deflections, for various values of index P, obtained by the Saint-Venant's solution. These deflections are compared with that of E-FGM beam. From this comparison (Fig. 35 and Table. 2), we observed that the S-FGM deflection when $P = 5$ is very close to E-FGM deflection. Table. 2 illustrates also a comparison between the non-dimensional deflections at mid-span of S-FGM beam and these of other FGM beams (P-FGM, E-FGM, and M-FGM).

Fig. 36 shows the 3D Saint-Venant's axial stress field computed on a cross-section at mid-span of the S-FGM beam. It can be noted that the shape of the 3D stress field is not plane and does not pass through the middle axis of cross-section (x-axis).

We present also in Fig. 37 the trends of the axial stresses at $x = 0$ (cut of 3D axial stress field shown in Fig. 36 at $x = 0$), for various values of index P. It can seen that the trend of the axial stress of S-FGM beam, with P = 1, is very close to that of E-FGM beam. The Table.3 shows also a comparison between the axial stress fields of S-FGM and those of other FGM beams (P-FGM, E-FGM, and M-FGM).

The 3D Saint-Venant's shear stress field of S-FGM beam when $P = 5$ is shown in Fig. 38. It is observed form this figure that the maximum value of the shear stress is occurs at $y/h = -0.15$ (see also Fig. 39).

The trends of the shear stresses at $x = -b/2$, extracted from the three-dimensional shear stress for various values of index P, are show in Fig. 39, it can be observed that the distributions of the shear stresses are not parabolic excepted for beam made of pure material.

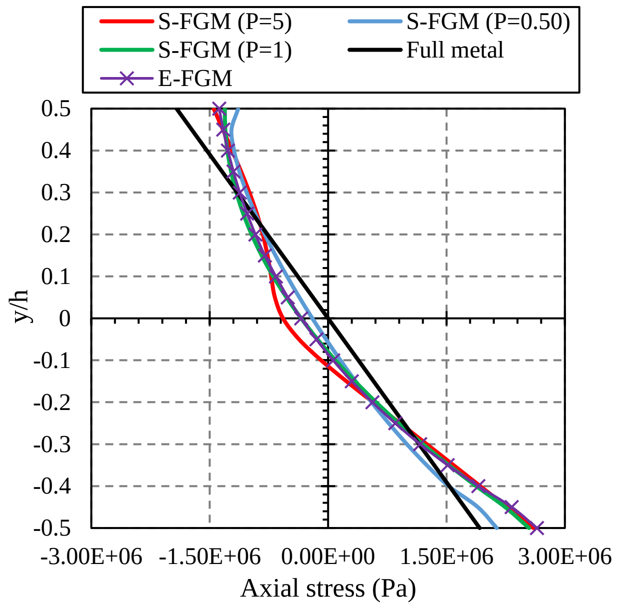

Fig. 37 Axial stress distributions obtained by SVBT at $x = -b/2$

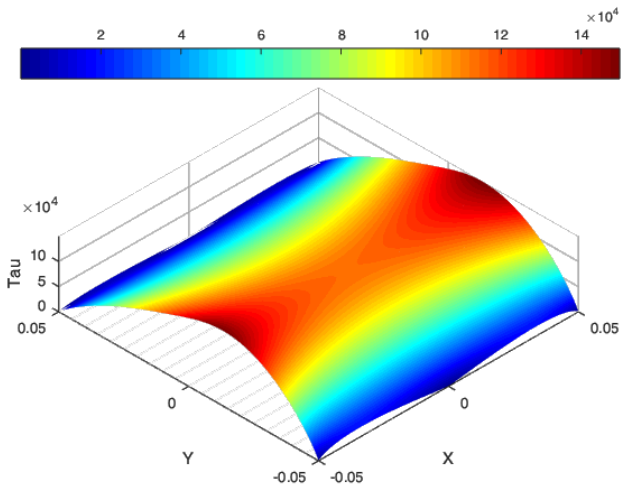

$-7.702Pa \le \tau \le 1.496e5\ Pa$
Fig. 38 Shear stress distribution of S–FGM beam (P=5)

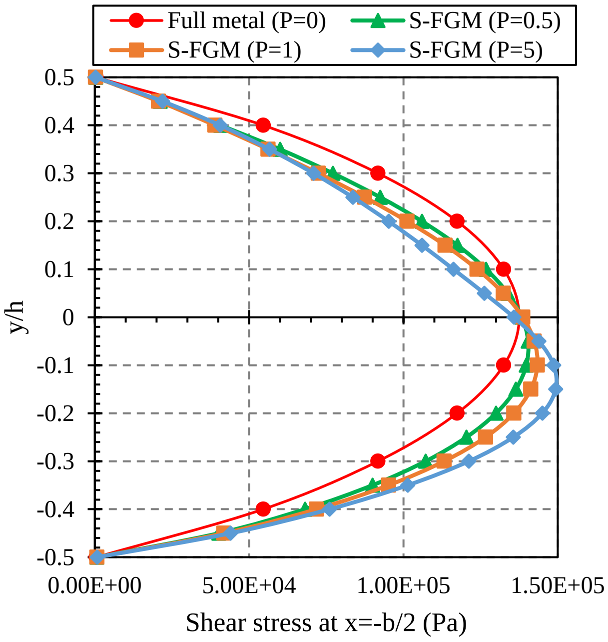

Fig. 39 Shear stress distributions at $x = -b/2$ of S-FGM beams

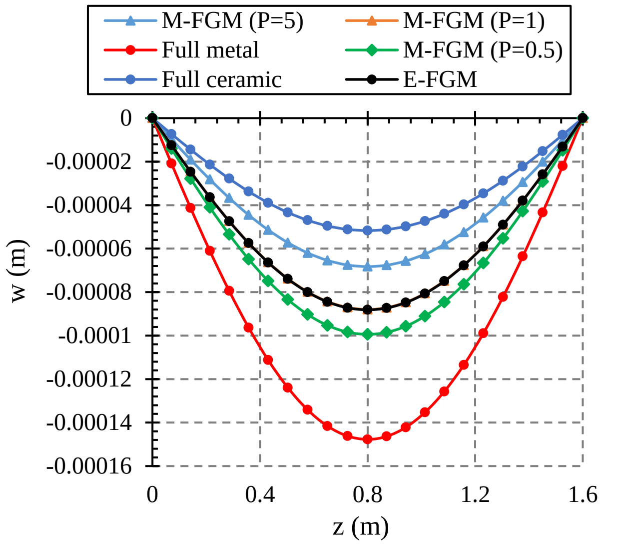

Fig. 40 Comparison between M-FGM and E–FGM deflections obtained by Saint-Venant theory.

5.2.4 Modelling of the M-FGM beam

Finally, we study the behaviour of the previous beam, considering now that its materials are varied according to Mori-Tanaka schema (M-FGM). The variation of Young's modulus through the dimensionless thickness of this M-FGM beam is illustrated in Fig. 4 (Section 2). The M-FGM beam is modelled in this paper by the 3D Saint-Venant's beam theory.

The numerical results obtained show that the deflection of M-FGM beam when $P = 1$ is identically to that of E-FGM (see Fig. 40 and Table. 2). A comparison between the non-dimensional deflections at mid-span of M-FGM beam and those of other FGM beams are present in Table. 2.

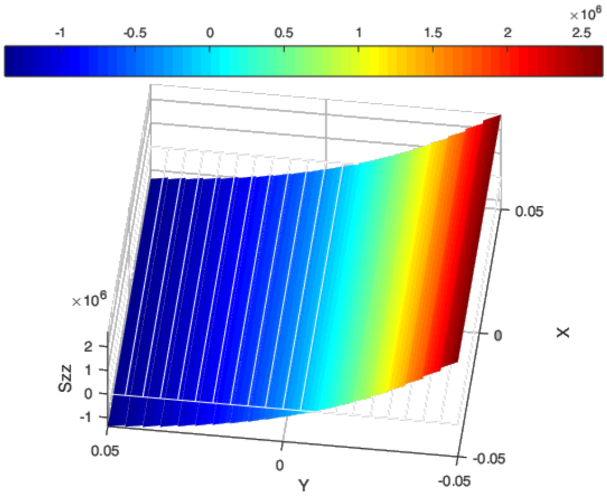

$-1.376e6Pa \leq \sigma_{zz} \leq 2.641e6\ Pa$

Fig. 41 Axial stress distribution of M–FGM beam (P=1)

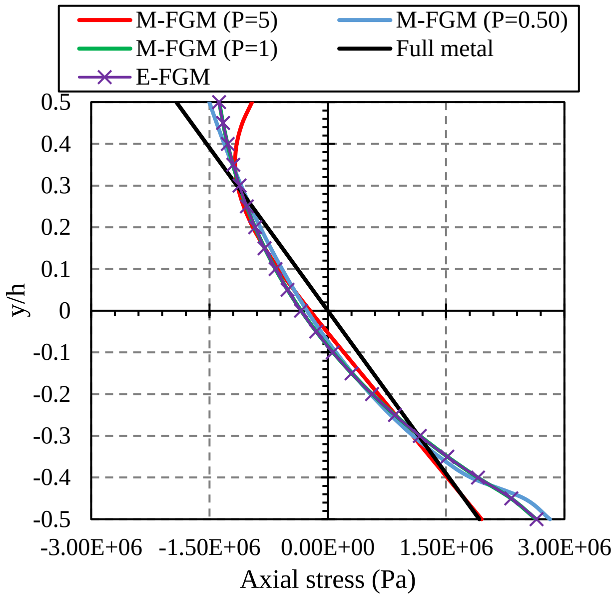

Fig. 42 Axial stress distributions obtained by SVBT

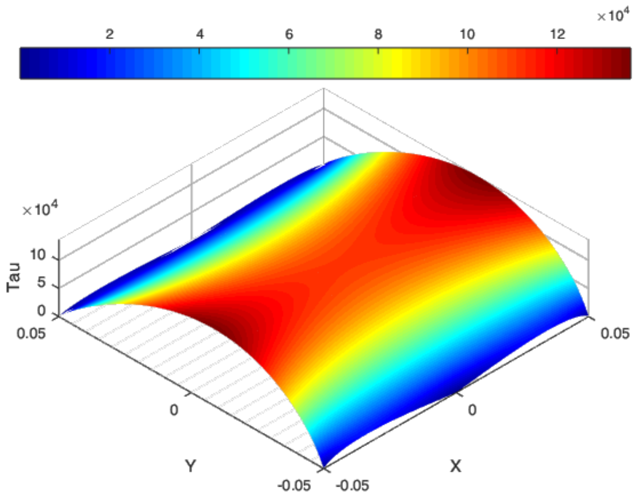

$8.551Pa \leq \tau \leq 1.364e5\ Pa$

Fig. 43 Shear stress distribution of M–FGM beam (P=1)

Table 3 Axial stress distribution obtained by various FGM beams (Pa)

y/h	Full metal	P-FGM			E-FGM	S-FGM			M-FGM		
		P=0.5	P=1	P=5	/	P=0.5	P=1	P=5	P=0.5	P=1	P=5
0.05	-1.92E+6	-1,46E+6	-1,36E+6	-1,11E+6	-1,38E+6	-1,14E+6	-1,31E+6	-1,45E+6	-1,50E+6	-1,38E+6	-9,61E+5
0.04		-1,32E+6	-1,32E+6	-1,42E+6	-1,27E+6	-1,22E+6	-1,30E+6	-1,33E+6	-1,41E+6	-1,33E+6	-1,08E+6
0.03		-1,14E+6	-1,20E+6	-1,36E+6	-1,12E+6	-1,19E+6	-1,28E+6	-1,22E+6	-1,31E+6	-1,27E+6	-1,16E+6
0.02		-9,13E+5	-9,93E+5	-1,07E+6	-9,21E+5	-1,12E+6	-1,23E+6	-1,10E+6	-1,21E+6	-1,20E+6	-1,18E+6
0.01		-6,36E+5	-7,10E+5	-6,65E+5	-6,62E+5	-1,03E+6	-1,16E+6	-9,97E+5	-1,10E+6	-1,12E+6	-1,14E+6
0		-3,03E+5	-3,46E+5	-2,07E+5	-3,42E+5	-9,24E+5	-1,08E+6	-9,03E+5	-9,82E+5	-1,03E+6	-1,07E+6
-0.01		9,39E+4	9,77E+4	2,72E+5	6,35E+4	-8,02E+5	-9,69E+5	-8,27E+5	-8,57E+5	-9,22E+5	-9,49E+5
-0.02		5,69E+5	6,21E+5	7,56E+5	5,62E+5	-6,66E+5	-8,42E+5	-7,67E+5	-7,23E+5	-8,01E+5	-7,99E+5
-0.03		1,15E+6	1,23E+6	1,24E+6	1,17E+6	-5,20E+5	-6,95E+5	-7,21E+5	-5,81E+5	-6,64E+5	-6,24E+5
-0.04		1,99E+6	1,91E+6	1,72E+6	1,90E+6	-3,64E+5	-5,28E+5	-6,74E+5	-4,28E+5	-5,10E+5	-4,30E+5
-0.05	1.92E+6	2,61E+6	2,50E+6	-1,11E+6	-1,38E+6	-1,99E+5	-3,41E+5	-5,71E+5	-2,64E+5	-3,38E+5	-2,26E+5

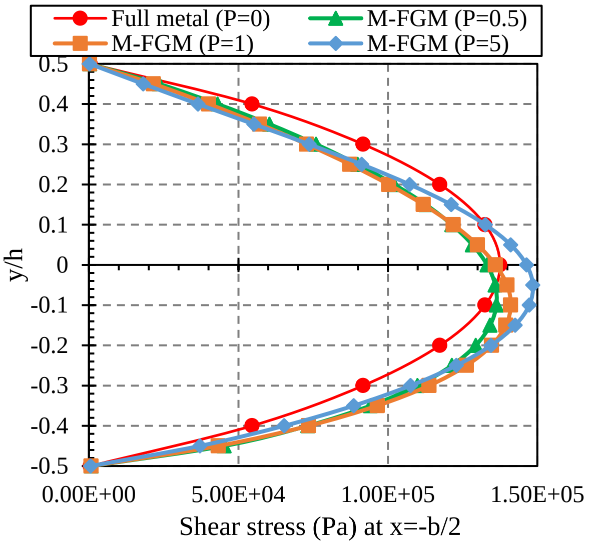

Fig. 44 Shear stress distributions at $x = -b/2$ of M-FGM beams

We noted also that the 3D axial stress of M-FGM when $P = 1$ (Fig. 41) is the same of E-FGM beam (see Fig.31). In order to facilitate the comparison between the axial stresses of M-FGM beam for various index P and these of E-FGM, we represent in Fig. 42 the trend of axial stress distribution at $x = 0$, the agreement between the results of M-FGM beam when $P = 1$ and that of E-FGM is clearly observed.

Table. 3 illustrates the axial stress distribution through non-dimensional thickness, y/h, at middle axis ($x = 0$) of the section and at mid-span of the beams ($z = L/2$), obtained for various FGM beams (P-FGM, E-FGM, S-FGM, and M-FGM). These values are extracted from the three-dimensional axial stress field obtained by Saint-Venant's theory. The comparison of these results shows that the axial stress of E-FGM beam is close to that of P-FGM beam when $P = 0.5$ ant $P = 1$. We noted also that the axial stress of E-FGM beam is very close, on one hand to that of S-FGM beam with $P = 1$, and on other hand to that of M-FGM beam when $P = 1$.

The 3D shear stress field of the M-FGM when $P = 1$, is plotted in Fig.43. From the set of three-dimensional shear stress fields of the M-FGM beam obtained for various values of the index P, we extracted their trends at $x = -b/2$ (Fig. 44). We clearly observed that these trends are asymmetric about the mid-plane of the beam (Fig. 44 shows that the maximum shear stress value for the case of $P = 1$ is occurs at $y/h = -0.1$).

6. Conclusions

In present paper, we study the mechanical behaviour of functionally graded materials beam using the 3D Saint-Venant's beam theory, in which the kinematic model includes sectional Poisson's effects and out-of plane warpings. Various functions are used for distribution of mechanical properties through the thickness of FGM beam. A numerical application in the literature were studied in order to validate our results obtained by 3D Saint-Venant's beam theory. In this application, we studied the behaviour of a simply supported FGM beam subjected to a uniformly distributed load. According to this application, it was noted that:

- 3D sectional stress fields of FGM beam are well described by the Saint-Venant's beam theory.
- A good agreement exists between the deflections obtained by our investigation and those obtained by other models in the literature (mainly for the P-FGM beam).
- A good agreement exists between the axial stress distribution at mid-span obtained by our investigation and those obtained by other models in the literature (mainly for the P-FGM beam).

References

Belabed, Z., Houari, M.S.A., Tounsi, A., Mahmoud, S.R. and Anwar Bég, O.A. (2014), "An efficient and simple higher order shear and normal deformation theory for functionally graded material (FGM) plates", *Compos. Part B*, **60**, 274-283.

https://doi.org/10.1016/j.compositesb.2013.12.057.

Ben-Oumrane, S., Tounsi, A., Mechab, I., Bachir, B.M., Meradjah, M. and Adda, B.E.A. (2009), "A theoretical analysis of flexional bending of Al/Al_2O_3 S-FGM thick beams", *Comput. Mater. Sci.*, **44**, 1344-1350. https://doi.org/10.1016/j.commatsci.2008.09.001.

Delale, F. and Erdogan, F. (1983), "The crack problem for a nonhomogeneous plane", *J. Appl. Mech*, **50**(3), 609-614. https://doi.org/10.1115/1.3167098.

Ebrahimi, F. and Barati, M.R. (2017), "Vibration analysis of embedded size dependent FG nanobeams based on third-order shear deformation beam theory", *Struct. Eng. Mech.*, **61**(6), 721-736. https://doi.org/10.12989/sem.2017.61.6.721.

El Fatmi, R. (2012), "A Matlab tool to compute the mechanical characteristics of any composite section". *Revue des Composites et des Matériaux Avancés*, **3**, 395-413.

El Fatmi, R. (2016), "A Refined 1D beam theory built on 3D saint-venant's solution to compute homogeneous and composite beams", *J. Mech. Mat.Struct.*, **11**(4), 345-378. https://doi.org/ 10.2140/jomms.2016.11.345.

El Fatmi, R. (2018), "Manuel de l'utilisateur du code", *CSB Cross-section & beam analysis*.

El Fatmi, R. and Zenzri, H. (2002), "On the structural behavior and the Saint Venant solution in the exact beam theory Application to laminated composite beams", *Comput. Struct.*, **80**, 1441-1456. https://doi.org/10.1016/S0045-7949(02)00090-1.

Filippi, M., Carrera, E. and Zenkour, A.M. (2015), "Static analyses of FGM beams by various theories and finite elements", *Compos. Part B*, **72**, 1-9. https://doi.org/10.1016/j.compositesb.2014.12.004.

Guenfoud, H. (2019), "Modélisation par éléments finis spéciaux des structures en matériaux à gradient fonctionnel", Ph.D. Dissertation, University of 8 Mai 1945, Guelma, Algeria.

Guenfoud, H., Ziou, H., Himeur, M. and Guenfoud, M. (2016), "Analyses of a composite functionally graded material beam with a new transverse shear deformation function", *J. Appl. Eng. Sci. Technol.*, **2**(2), 105-113. http://revues.univ-biskra.dz/index.php/jaest/article/view/1898.

Hadji, L., Daouadji, T. H., Meziane, M. A. A., Tlidji, Y. and Bedia, E. A. A. (2016), "Analysis of functionally graded beam using a new first-order shear deformation theory". *Struct. Eng. Mech.*, **57**(2), 315-325. http://dx.doi.org/10.12989/sem.2016.57.2.315.

Hajmohammad, M.H., Zarei, M.S., Nouri, A. and Kolahchi, R. (2017), "Dynamic buckling of sensor/functionally graded-carbon nanotube reinforced laminated plates/actuator based on sinusoidal-viscopiezoelasticity theories", *J. Sandwich Struct. Mater.* **0**(00) 1–33. https://doi.org/10.1177/1099636217720373.

Hosseini, H. and Kolahchi, R. (2018), "Seismic response of functionally graded-carbon nanotubes-reinforced submerged viscoelastic cylindrical shell in hygrothermal environment", *Physica E Low diemnsion. Syst. Nanostruct.*, **102**, 101-109. https://doi.org/10.1016/j.physe.2018.04.037.

Kaci, A., Belakhdar, K., Tounsi, A. and Bedia, E. A. A. (2014), "Nonlinear cylindrical bending analysis of E-FGM plates with variable thickness", *Steel Compos. Struct.*, **16**(4), 339-356. be.khalil@gmail.com.

Karami, B., Janghorban, M. and Tounsi, A. (2017), "Effects of triaxial magnetic field on the anisotropic nanoplates", *Steel Compos. Struct.*, **25**(3), 361-374. https://doi.org/10.12989/scs.2017.25.3.361.

Karami, B., Janghorban, M. and Tounsi, A. (2018b) "Nonlocal strain gradient 3D elasticity theory for anisotropic spherical nanoparticles", *Steel Compos. Struct.*, **27**(2), 201-216. https://doi.org/10.12989/scs.2018.27.2.201.

Karami, B., Janghorban, M., Shahsavari, D. and Tounsi, A. (2018c), "A size-dependent quasi-3D model for wave dispersion analysis of FG nanoplates", *Steel Compos. Struct.*, **28**(1), 99-110. https://doi.org/10.12989/scs.2018.28.1.099.

Karami, B., Shahsavari, D., Nazemosadat, S. M. R., LI, L. and Ebrahimi, A. (2018a), "Thermal buckling of smart porous functionally graded nanobeam rested on Kerr foundation", *Steel Compos. Struct.* **29**(3), 349-362. https://doi.org/10.12989/scs.2018.29.3.349.

Khebizi M, Guenfoud H. and Guenfoud M. (2018), "Numerical modelling of soil-foundation interaction by a new non–linear macro–element", *Geomech. Eng.*, **14(**4), 377-386. https://doi.org/10.12989/gae.2018.14.4.000.

Khebizi M. and Guenfoud M. (2015), "Numerical modelling of the damaging behaviour of the reinforced concrete structures by multi-layers beams elements", *Comput. Concrete*, **15**(4), 547-562.

Khebizi M., Guenfoud H. and Guenfoud M. (2018), "Contribution to the damage modelling of reinforced concrete structures", *MATEC Web of Conferences*, **149**. https://doi.org/10.1051/matecconf/201814901052.

Kolahchi, R., Zarei, M. S., Hajmohammad, M. H., Nouri, A., (2017), "Wave propagation of embedded viscoelastic FG-CNT-reinforced sandwich plates integrated with sensor and actuator based on refined zigzag theory", *J. Mech. Sci.*, **130**, 534-545. https://doi.org/10.1016/j.ijmecsci.2017.06.039.

Kolahchi, R., Bidgoli, A. M. M. and Heydari, M. M. (2015), "Size-dependent bending analysis of FGM nano-sinusoidal plates resting on orthotropic elastic medium", *Struct. Eng. Mech.*, **55**(5), 1001-1014. http://dx.doi.org/10.12989/sem.2015.55.5.1001.

Kolahchi, R., Keshtegar, B., Fakhar, M. H. (2017), "Optimization of dynamic buckling for sandwich nanocomposite plates with sensor and actuator layer based on sinusoidal-visco-piezoelasticity theories using Grey Wolf algorithm", *J. Sandwich Struct. Mater.*, **0**(00) 1–25. https://doi.org/10.1177/1099636217731071.

Kolahchi, R., Safari, M., Esmailpour, M. (2016), "Dynamic stability analysis of temperature-dependent functionally graded CNT-reinforced visco-plates resting on orthotropic elastomeric medium", *Compos. Struct.*, **150**, 255-265. https://doi.org/10.1016/j.compstruct.2016.05.023.

Ladevère, P. and Simmmonds, J. (1998), "Nous concepts for linear beam theory with arbitrary geometry and loading", *Europ. J. Mech. A Solid.*, **17** (3), 377-402. https://doi.org/10.1016/S0997-7538(98)80051-X.

Lahmar, M. (2017), "Equilibre thermo-élastique d'une poutre de section composite quelconque", Ph.D. Dissertation, El Manar University, Tunis.

Lee, C.Y. and Kim, J.H. (2013), "Thermal post-buckling and snap-through instabilities of FGM panels in hypersonic flows", *Aerosp. Sci. Technol.*, **30**, 175-182. https://doi.org/10.1016/j.ast.2013.08.001.

Madani, H., Hosseini, H. and Shokravi, M. (2016), "Differential cubature method for vibration analysis of embedded FG-CNT-reinforced piezoelectric cylindrical shells subjected to uniform and non-uniform temperature distributions", *Steel and Compos. Struct.*, **22**(4), 889-913. https://doi.org/10.12989/scs.2016.22.4.889.

Naccache, F. and El-Fatmi, R. (2018), "Buckling analysis of homogeneous or composite I-beams using a 1D refined beam theory built on Saint Venant's solution", *Thin-Walled Struct.*, **127**, 822-831. https://doi.org/10.1016/j.tws.2018.02.028.

Nejad, M.Z., Hadi, A., Omidavari, A. and Rastgoo, A. (2018), "Bending analysis of bi-directional functionally graded Euler-Bernoulli nano-beams using integral form of Eringen's non-local elasticity theory", *Struct. Eng. Mech.*, **67**(4), 417-425. https://doi.org/10.12989/sem.2018.67.4.417.

Pradhan, K.K. and Chakraverty, S. (2013), "Free vibration of Euler and Timoshenko functionally graded beams by Rayleigh–Ritz method", *Compos. Part B*, **51**, 175–184. https://doi.org/10.1016/j.compositesb.2013.02.027.

Sankar, B.V. (2001) "An elasticity solution for functionally graded beams", *Compos. Sci. Technol.*, **61**, 689-696. https://doi.org/10.1016/S0266-3538(01)00007-0.

Şimşek, M. (2009), "Static analysis of a functionally graded beam under a uniformly distributed load by Ritz method", *Int. J. of Eng. Appl. Sci.*, **1**(3), 1-11.
Zenkour, A. M. (2007), "Benchmark trigonometric and 3-D elasticity solutions for an exponentially graded thick rectangular plate", *Arch. Appl. Mech.*, **77**(4), 197-214. https://doi.org/10.1007/s00419-006-0084-y.
Zenkour, A.M. (2006), "Generalized shear deformation theory for bending analysis of functionally graded plates", *Appl. Math. Modelling*, **30**, 67-84. https://doi.org/10.1016/j.apm.2005.03.009.
Ziou, H. (2017), "Contribution à la modélisation des structures en Matériaux à Gradient Fonctionnel", Ph.D. Dissertation, Mohamed Khider University, Biskra, Algeria.
Ziou, H., Guenfoud, H. and Guenfoud, M. (2016), "Numerical modelling of a Timoshenko FGM beam using the finite element method", *Struct. Eng.*, **7**(3), 239-261.
Ziou, H., Guenfoud, H., Himeur, M. and Guenfoud, M. (2017a), "Numerical modeling of a Timoshenko FGM beam using the finite element method", *Courrier du Savoir*, **24**, 59-66.
Ziou, H., Guenfoud, H., Himeur, M., and Guenfoud, M. (2017b), "An efficient finite element model for vibration analysis of the FGM nonlocal based on Euler–Bernoulli beam theory", *Congrès Algérien de Mécanique,* Constantine*,* Algeria, 26-30 November.

CC